Research Article | Vol. 29, No. 20 / 27 Sep 2021 / Optics Express 32453
Optics EXPRESS

High-precision photonic crystal fiber-based pressure sensor with low-temperature sensitivity

YANJIN ZHAO, NINGFANG SONG, FUYU GAO,* XIAOBIN XU, JIAQI LIU, AND CHENCHEN LIU

School of Intrument Science and Opto-Electronic Engineering, Beihang University, Beijing 100191, China
*467835587@qq.com

Abstract: A novel high-precision photonic crystal fiber-based pressure sensor with low-temperature sensitivity is proposed. The sensor is fabricated by fusion splicing a photonic crystal fiber with a hollow core fiber immersed in polydimethylsiloxane. Owing to the special structure of the photonic crystal fiber, the temperature cross-coupling effect can be minimized and the membrane shape can be controlled. Experimental results indicate that the pressure sensitivity of the FP pressure sensor is 2.47 nm/kPa, 5.37 times the temperature sensitivity of 0.46 nm/°C. The proposed FP pressure sensor has broad application prospects in chemical and biological detection for monitoring pressure in real time.

1. Introduction

Fiber optical sensors with a Fabry–Pérot (FP) cavity structure have attracted considerable research attention because of their simple structure, low cost, electromagnetic immunity, fast response time, and high sensitivity, which can be applied in oil exploration, medical diagnosis, and industrial production [1]. In previous studies, many novel fiber optical FP pressure sensors were proposed to meet requirements in temperature and pressure measurements [2–8]. Many fiber optical FP pressure sensors were developed based on long-period gratings, [9] hollow microsphere cavities, [10] and hybrid fiber structures [11]. The most common structure is based on a silicon material with good biocompatibility and long-term stability; however, the production process requires expensive equipment and precise control. The FP pressure sensors with polymer membranes have become an attractive choice because of their low Young's modulus and simple curing progress to realize simple production and high sensitivity. A submicron thin film can be easily obtained by photolithography [12], UV imprinting lithography [13], or other conventional polymer techniques [14,15]. All of the above FP pressure sensors have a large temperature cross-coupling effect, and a small temperature change can cause inaccuracies in the pressure measurement.

The temperature sensitivity of the fiber optical FP pressure sensors is attributed to the large thermal expansion of the material and air. The most common approach to eliminate the temperature coupling effect and obtain higher accuracy pressure measurements is measuring the pressure and temperature simultaneously. Among them, the use of a fiber Bragg grating (FBG) or another FP sensor as a temperature sensor and an extrinsic FP interferometric sensor as a pressure sensor have been studied and proved to be useful. The all-fused extrinsic FP interferometric pressure and FBG sensors are on the same fiber and placed at the measurement point with pressure and temperature sensitivities of 1.685 nm/kPa and 1.7 nm/°C, respectively [16]. The pressure and temperature are simultaneously obtained using two separate FP sensors [17,18]; the pressure sensor comprises a cavity covered by a composite membrane, and the temperature sensor comprises an intrinsic cavity. The pressure and temperature sensitivities of the all-silica FP fiber optic sensor were measured to be 3.97 nm/kPa and 6.8 nm/°C, respectively [19].

#433248 https://doi.org/10.1364/OE.433248
Journal © 2021 Received 17 Jun 2021; revised 2 Sep 2021; accepted 6 Sep 2021; published 24 Sep 2021

Optics EXPRESS

In this study, a novel high-precision photonic crystal fiber-based pressure sensor with low temperature sensitivity was proposed; this sensor has advantages of easy fabrication, good biocompatibility, fast response, and high precision. The experimental results indicate that the FP pressure sensors based on the PCF-HCF structure can more accurately reduce the temperature coupling effect during the pressure measurement.

2. Principle of the sensor

The schematic of the sensor is shown in Fig. 1. The first, second, and third reflecting surfaces R_1, R_2, and R_3 are formed when light enters the PCF and transmits to the first splicing point (the end of the PCF), after light passes through the FP air cavity, and when light reaches the outer interface of the polymer membrane, respectively.

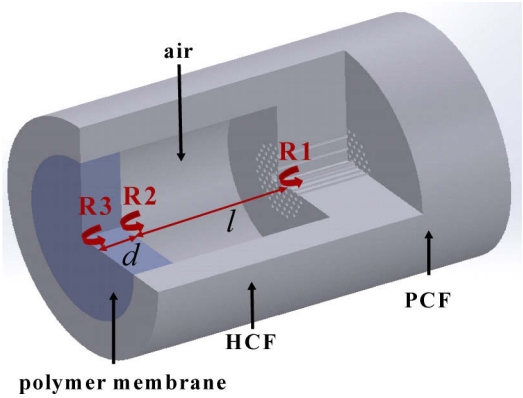

Fig. 1. Schematic of Fabry–Pérot (FP) pressure sensor

The reflectivity of the three reflecting surfaces can be calculated using the Fresnel reflection equation; the refractive indices of air, fiber, and polymer are n_0, n_1, and n_2, respectively.

$$R_1 = \left(\frac{n_1 - n_0}{n_1 + n_0}\right)^2, R_2 = R_3 = \left(\frac{n_2 - n_0}{n_2 + n_0}\right)^2 \tag{1}$$

Higher-order reflections from these surfaces are neglected because the interface reflectivity of silica/air and polymer/air interface is lower than 3.5%. A two-wave interference model can be used because of the thin membrane and the large loss of light transmissions caused by the membrane material; the combined reflected electric field E_r can be expressed as

$$E_r = E_i[R_1 + A^2 + 2\sqrt{R_1}A\cos(2\phi)]$$

$$\phi = \frac{4\pi n_1 l}{\lambda}$$

$$A = (1 - R_1)\sqrt{R_2} \tag{2}$$

where *Ei* and *Er* represent the input electric field and reflected electric field, respectively; Φ denotes the light phase delay caused by the air cavity; *l* denotes the length of the air cavity; λ represents the wavelength of the input light.

The wavelength shift may be described by [20]

$$\Delta\lambda = \lambda \cdot \frac{\Delta l}{l} \tag{3}$$

Optics EXPRESS

2.1. Pressure sensing

The membrane is deformed when pressure is applied, and it leads to a change in the cavity length. Based on von Kamen's thin plate theory, the pressure sensitivity of the proposed FP pressure sensor based on a uniform circular membrane can be expressed as [21]

$$\frac{\Delta l}{\Delta P} = \frac{3(1-\mu^2)r^4}{16Ed^3} \tag{4}$$

where E and μ denote the Young's modulus and Poisson's ratio of the membrane material, ΔP denotes the imposed pressure, and d and r represents the thickness and radius of the membrane, respectively. As indicated by Eq. (4), a material with a low Young's modulus and a small thickness-to-diameter ratio of the membrane can enhance the pressure sensitivity of the FP pressure sensor.

The membrane of the proposed FP pressure sensor comprises a polymer material with a low thermal expansion and low elastic modulus. A simulation model of the FP pressure sensor based on different membrane shapes is designed to further investigate the effect of the structural parameters of irregularly shaped diaphragms on pressure sensitivity. The membrane shape is divided into convex (inner and outer surfaces of the membrane are convex), plano-concave (inner surface of the membrane is concave and outer surface is plano), and concave types (both inner and outer surfaces of the membrane are concave), as shown in Fig. 2.

The simulation results indicate that when the thickness at the center of the membrane and cavity length are the same, and the pressure measurement sensitivity of the FP cavity sensor based on the convex membrane is the highest at 2.70 nm/kPa, followed by 2.10 nm/kPa and 1.72 nm/kPa, respectively, for the plano-concave and concave types, as shown in Fig. 3.

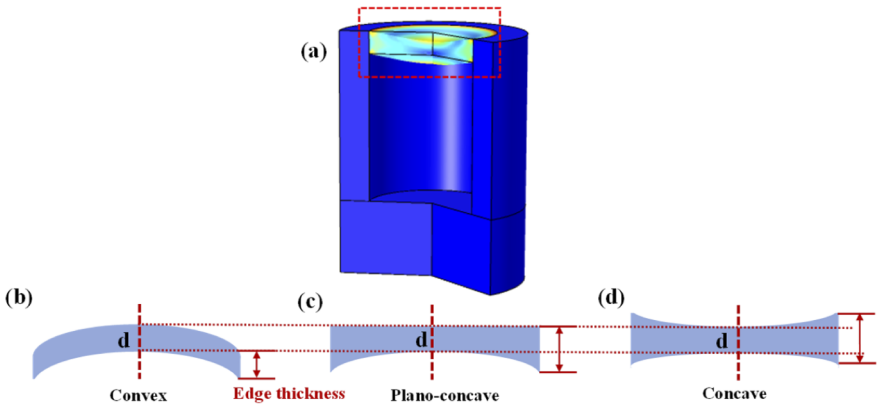

Fig. 2. Different membrane shapes. (a) Simulation of the pressure sensor; (b) Axial section view of convex membrane; (c) Axial section view of plano-concave membrane; (d) Axial section view of concave membrane.

Indeed, the shape of the membrane has a significant effect on the pressure measurement sensitivity of the optical fiber FP pressure sensors. By comparing these three types of membranes, a reasonable explanation for this result is that the edge thickness of the membrane shapes affects the sensitivity of the sensors. The edge area of the convex membrane has less polymers attached to the inner surface of the HCF than the other two shapes, which makes this shape more easily deformed. Further, as shown in Fig. 4, the influence of the increasing membrane edge thickness on sensor performance was investigated and simulated; this indicates that an increase in the edge thickness of 1 μm causes the pressure sensitivity to decrease to 0.3nm/kPa. The edge thickness of the concave type is set to be 2um more than that of the plano-concave type and 3.3um more

Optics EXPRESS

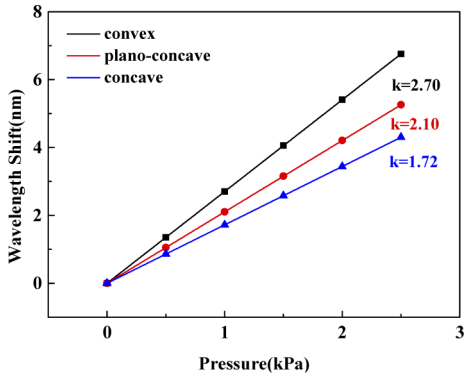

Fig. 3. Simulation analyses of the pressure sensing performance of the sensor based on three different types of membrane

than that of the convex type. According to the simulation results, the sensitivity will be reduced by 0.6nm/kPa and 0.99 nm/kPa, which are similar to the previous simulation results and makes the sensor based on a convex-type membrane the most suitable for pressure sensing.

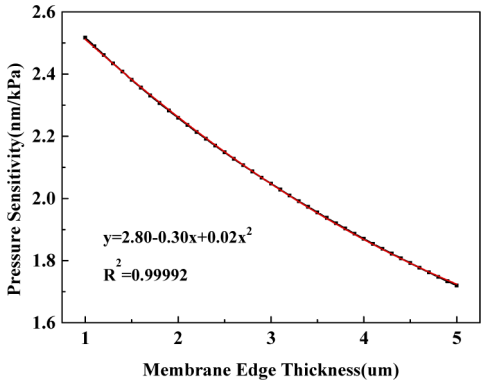

Fig. 4. Relationship between wavelength shift and membrane edge thickness

2.2. Temperature cross-coupling

The pressure sensitivity of the sensor may be degraded because of the mismatch in the thermal expansion coefficient of the different components. When the temperature changes, the cavity length changes with the expansion and contraction of the air in the cavity instead of being affected by the thermal expansion coefficient of the membrane, which is an order of magnitude less than that of the air. From the ideal gas equation, an increase (decrease) in the temperature of the gas in the closed space can cause an increase (decrease) in the pressure in the cavity, and this can lead to the temperature cross-coupling of the FP pressure sensor. Assuming that the volume of the gas is constant, the relationship between the pressure imposed on the membrane and the temperature can be derived from the ideal gas equation. The temperature sensitivity of the proposed FP pressure sensor can be expressed as

$$\frac{\Delta\lambda}{\Delta T} = \frac{\lambda}{l} \cdot \frac{\Delta l}{\Delta T} = \frac{\lambda}{l} \cdot \frac{P_0}{T_0} \cdot \frac{\Delta l}{\Delta P} \tag{5}$$

Optics EXPRESS

where P_0 and T_0 denote the initial environmental parameters. As indicated in Eqs. (4) and (5), the deflection of the membrane caused by the changes in temperature depends linearly on the pressure sensitivity of the sensor under the condition of constant gas volume. Therefore, if air is always present in the cavity, simply increasing the pressure sensitivity will increase the temperature sensitivity correspondingly, which will not help eliminate the temperature coupling effect. The influence of the temperature cross-coupling of the FP pressure sensor can be decreased by reducing the air in the cavity.

A simulation model of the FP pressure sensor based on different membrane shapes at various temperatures was built. Figure 5 shows the temperature sensitivity of the FP cavity sensor with the same central thickness membrane based on the convex membrane is the highest of 0.53 nm/°C, followed by the plano-concave type of 0.43 nm/°C and the concave type of 0.35 nm/°C. A comparison of the sensing performance of the FP pressure sensors based on different membrane types is presented in Table 1.

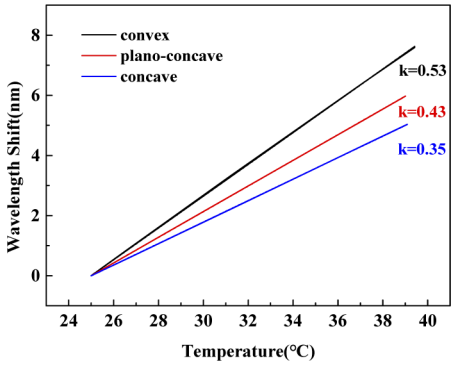

Fig. 5. Simulation analyses of the temperature sensing performance of the sensor based on three different types of membrane.

Table 1. Comparison of sensing performance of the FP pressure sensors based on different membrane types

Membrane type	Simulation pressure sensitivity	Simulation temperature sensitivity	Pressure-temperature ratio
Convex	2.70 nm/kPa	0.53 nm/°C	5.09
Plano-concave	2.10 nm/kPa	0.43 nm/°C	4.88
Concave	1.72 nm/kPa	0.35 nm/°C	4.91

As illustrated in Table 1, the FP cavity sensor based on the convex membrane presented a high pressure-temperature ratio of 5.09. The reason for the small pressure-temperature ratio difference may be attributed to the small change in the air in the cavity, which makes the temperature and pressure sensitivities nonlinear.

3. Fabrication of sensor

The fabrication stage of the sensor is illustrated in Fig. 6. First, one cleaved end of a standard single-mode fiber (SMF) flat was immersed into the polymer solution vertically and picked up quickly when it touched only the polymer solution to prevent excessive solution at the end; then, it was clamped on the fixture, as shown in Fig. 6(a). Second, as shown in Fig. 6(b), the prepared empty HCF structure was clamped by the left holder of the fixture. Third, the SMF was moved to the HCF through the motor of the adapter until the liquid was attached to the end surface of the HCF. Thus, the solution was immersed in an empty tube because of the capillary action. The

Optics EXPRESS

other pigtail of the PCF needs to be sealed in a gas chamber connected to an air pressure control device to prevent the solution from immersing too quickly because of the low viscosity of the solution; further, the air tightness of the connection needs to be guaranteed. An online spectral modulation system is required to obtain the appropriate transmission spectrum and modulate the cavity length of the FP sensor online.

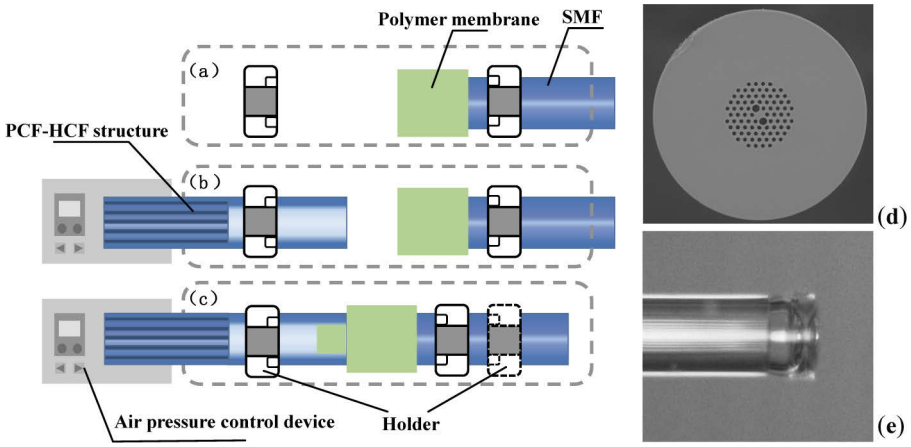

Fig. 6. Fabrication process of the polymer immersed fiber sensor. (a) First transfer step; (b) Second transfer step; (c) Polymer immersion; (d) Optical microscope image of cross section of photonic crystal fiber. (e) Optical microscope image of the proposed FP pressure sensor structure.

A schematic of the proposed FP pressure sensor immersed in a polymer is shown in Fig. 6(e). However, the high temperature generated during the splicing process can cause air holes inside the photonic crystal fiber to collapse, which leads to a high splicing loss. Light-collapse splicing between the PCF and HCF was achieved through precise splicing parameter settings.

The shape of the membrane depends on the air pressure inside the cavity, which can be adjusted by adjusting the air inlet velocity through the air holes of the PCF. The membrane material can be cured instantaneously when it is subjected to a sudden high temperature, so after adjusting the air pressure and curing at a high temperature, the shape of the membrane can be well adjusted and fixed. As shown in Fig. 7, a simulation of the membrane inner face distortion and air inlet velocity during the curing process of the membrane material was designed. The increase in the air inlet velocity results in the distortion of the inner membrane face to the outside, which can cause variations in the membrane shapes. According to the simulation results, a change in the inlet velocity of 1 m/s will caused the membrane to deform by 8 μm. Owing to the special air hole structure of the photonic crystal fiber, the air pressure in the FP cavity can be tuned by controlling the air in and out of the open port of the photonic crystal fiber, and therefore, the shape of the membrane changes because of the pressure difference between the inner and outer surfaces when the membrane is cured. From the experiment, the two surfaces are concave when the membrane is formed in a natural state (uncontrolled air pressure). When the air inlet viscosity in the open port is controlled to be 0.6 m/s through the photonic crystal fiber, the inner surface of the membrane is concave and the outer surface is plano. When the air inlet viscosity is 1.3 m/s, both surfaces of the membrane protrude out of the cavity, which is the convex type.

Optics EXPRESS

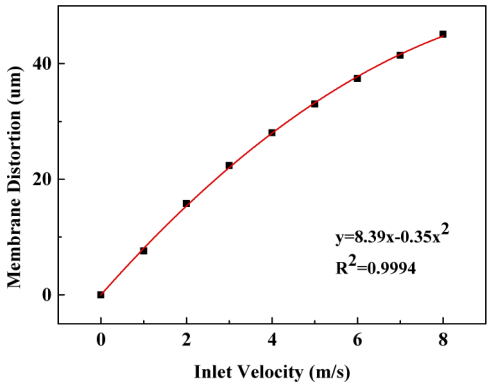

Fig. 7. Relationship between membrane distortion and inlet velocity obtained from simulation.

4. Results and discussion

Figure. 8 shows that the experimental system comprises a light source with a wavelength range of 1520–1580 nm(NKT Photonics), a circular FP pressure sensor, and an optical spectrum analyzer(YOKOGAWA AQ6370D) used to monitor and normalize the reflected output spectrum.

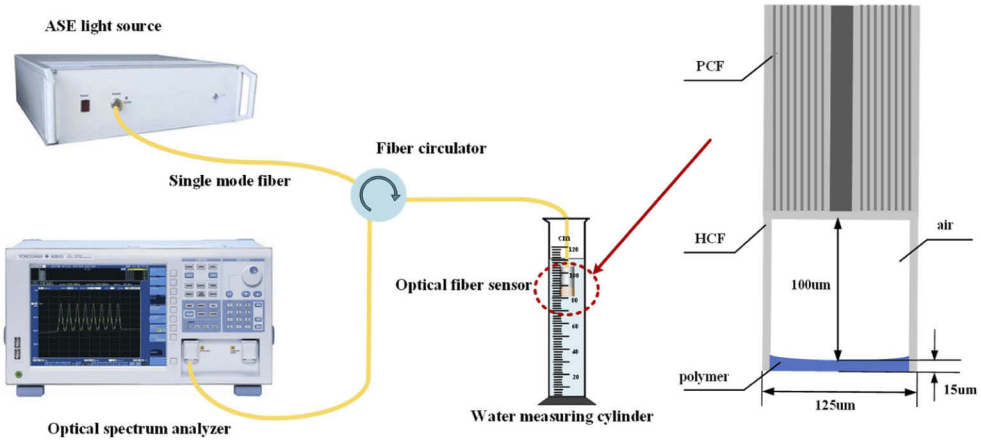

Fig. 8. Schematic of experimental device for measuring pressure sensitivity

In the pressure sensitivity experiment, the fiber tip was placed horizontally in a deep container filled with water, and the distance between the FP pressure sensor and water surface was proportional to the pressure applied to the membrane; the pressure was increased from 0 kPa to 2.5 kPa at a step size of 0.5 kPa. Consequently, the wavelength shifts to a shorter wavelength with increasing applied pressure. A linear fit of the experimental data is implemented after normalizing the central thickness of the membrane. Figure 9(a), (b), and (c) show diagrams of the FP pressure sensor based on plano-concave, convex, and concave membranes, respectively. Figure 9(d) shows the sensitivity of the FP pressure sensors based on the convex, plano-concave, and concave membranes is 2.47 nm/kPa, 2.04 nm/kPa, and 1.63 nm/kPa, respectively. The experimental results were lower than the simulation results. A possible reason for this difference between the simulation and experimental results is the irregularity of the membrane shape.

Optics EXPRESS

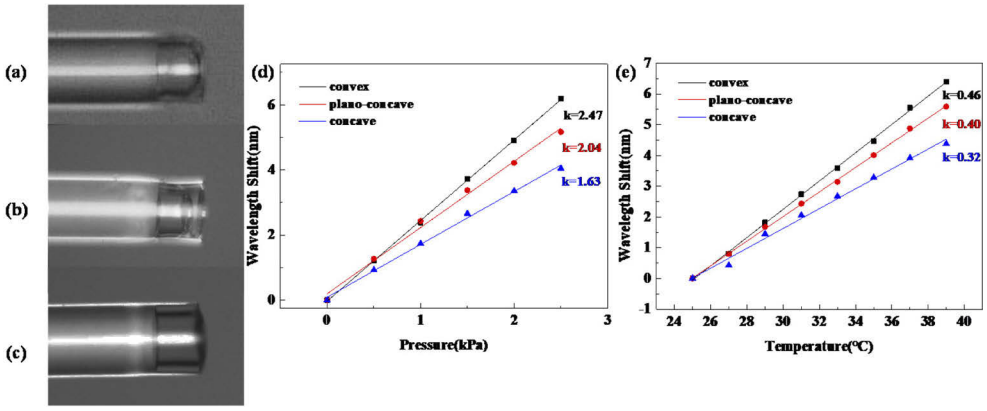

Fig. 9. Different membrane shapes (a) Plano-concave; (b) Convex; (c) Concave. (d) Experimental relationship between wavelength shift and pressure of three membrane shapes. (e) Experimental relationship between the wavelength shift and temperature of the three membrane shapes.

Under the same experimental equipment conditions, the FP pressure sensor was placed in the thermostat for a temperature measurement experiment. The temperature was raised from 25 °C to 39 °C at intervals of 1 °C. From the experimental results, the wavelength experiences the red shift and the temperature sensitivity of the EFPI is 0.46 nm/°C (convex), 0.4 nm/°C (plano-concave), and 0.32 nm/°C (concave), as shown in Fig. 9(e).

Table 2 indicates that the FP cavity based on a convex-type membrane is slightly helpful in improving the pressure sensing performance of our proposed structure; the pressure-temperature sensitivity ratio of the FP pressure sensor can be increased to 5.37.

Table 2. Comparison of the sensing performance of FP pressure sensors based on different membrane types

Membrane type	Experimental pressure sensitivity	Experimental temperature sensitivity	Pressure-temperature ratio
Convex	2.47 nm/kPa	0.46 nm/°C	5.37
Plano-concave	2.04 nm/kPa	0.40 nm/°C	5.10
Concave	1.63 nm/kPa	0.32 nm/°C	5.09

The comparative structure with the SMF-HCF structure FP pressure sensor was fabricated with the same parameters to verify that the PCF-HCF structure can significantly reduce the influence of temperature changes. The pressure measurement sensitivities of the two sensors based on different optical fiber structures remain the same by controlling the membrane thickness. The PCF-FP pressure sensor used for comparison uses a convex membrane, and the SMF-FP pressure sensor uses a concave membrane because the shape of the membrane cannot be adjusted. The temperature performance of the SMF-HCF FP pressure sensor was 2.92 nm/°C. Compared with the SMF-HCF structure, the pressure-temperature sensitivity ratio of the PCF-HCF structure is 6.35 times higher, as shown in Fig. 10. This proves that the FP pressure sensor based on the PCF-HCF structure is helpful in significantly reducing the influence of temperature on the pressure measurement.

A comparison of the temperature cross-sensing performances of the FP pressure sensors between our PCF-HCF FP pressure sensors and other recently reported schemes, which include the structure size, pressure sensing sensitivity values, and pressure-temperature sensitivity ratio, are listed in Table 3. As summarized in Table 3, the sensor based on the PCF-HCF structure has

Optics EXPRESS

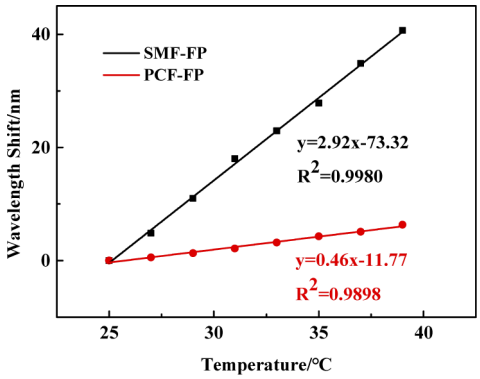

Fig. 10. Comparison of pressure sensing performance of FP pressure sensors based on PCF-HCF and SMF-HCF structure

a compact design and low-temperature cross-coupling effect, compared with many reported FP pressure sensors.

Table 3. Comparison of sensing performance of our sensor with recent reported schemes

Type	FPI cavity length or structure size	Pressure sensitivity	Temperature sensitivity	Ratio	Ref
FBG/EFPI hybrid sensor	Outer diameter 220 μm	1.685 nm/kPa	1.7 nm/°C	0.9912	[19]
Hybrid dual F-P cavity	Cavity length of 250 μm polymer thickness of 35 μm	12.2 nm/kPa	13.9 nm/°C	0.8777	[13]
Etched PCF FPI	Hole diameter of 60 μm	0.0000547 nm/kPa	0.00045 nm/°C	0.1216	[22]
Polymer capped	Polymer cap thickness of 12.7 μm	0.00113 nm/kPa	0.249 nm/°C	0.0045	[23]
Filled with POLY-MER	276 μm	0.06514 nm/kPa	0.0828 nm/°C	0.7867	[18]
PCF-HCF POLY-MER membrane	Cavity length of 100 μm	2.47 nm/kPa	0.46 nm/°C	5.37	This study

5. Conclusion

In this study, a novel high-precision photonic crystal fiber-based pressure sensor with low-temperature sensitivity was proposed. The low-temperature sensitivity can be attributed to the air hole structure of the photonic crystal fiber. The air can be exhausted through the air hole, which reduces the temperature sensitivity of the FP pressure sensor by six times to 0.42 nm/°C and maintains its pressure sensitivity at a high level to avoid the thermal expansion and contraction effect of the air in the cavity during the process of air heating and cooling. Further, the results of

Optics EXPRESS

this experiment show that the shape of the polymer membrane in this sensor can be changed by precisely controlling the air pressure in the cavity through the photonic crystal fiber. Compared with the previous concave type, the FP pressure sensor based on convex membrane obtained in this paper can reach 2.47 nm/kPa, and this can greatly improve the pressure sensitivity and achieve the high pressure-temperature ratio of 5.37. Our proposed FP pressure sensor has the desirable merits of flexible design, small scale, and high sensitivity because of the low-temperature cross-coupling; it is anticipated in pressure monitoring in certain temperature-fluctuating environments.

Funding. National Natural Science Foundation of China (61575012, 61575013, 61935002).

Disclosures. The authors declare that there are no conflicts of interest related to this article.

Data availability. Data underlying the results presented in this paper may be available from the corresponding author upon reasonable request.

References

1. S. Liu, Y. Wang, C. Liao, G. Wang, Z. Li, Q. Wang, J. Zhou, K. Yang, X. Zhong, J. Zhao, and J. Tang, "High-sensitivity strain sensor based on in-fiber improved Fabry–Perot interferometer," Opt. Lett. **39**(7), 2121–2124 (2014).
2. C. Liao, Q. Wang, L. Xu, S. Liu, J. He, J. Zhao, Z. Li, and Y. Wang, "D-shaped fiber grating refractive index sensor induced by an ultrashort pulse laser," Appl. Opt. **55**(7), 1525–1529 (2016).
3. J. H. Liou and C. P. Yu, "All-fiber Mach-Zehnder interferometer based on two liquid infiltrations in a photonic crystal fiber," Opt. Express **23**(5), 6946–6951 (2015).
4. G. Yan, Y. Liang, E.-H. Lee, and S. He, "Novel Knob-Integrated fiber Bragg grating sensor with polyvinyl alcohol coating for simultaneous relative humidity and temperature measurement," Opt. Express **23**(12), 15624–15634 (2015).
5. Z. Xu, Q. Sun, B. Li, Y. Luo, W. Lu, D. Liu, P. P. Shum, and L. Zhang, "Highly sensitive refractive index sensor based on cascaded microfiber knots with Vernier effect," Opt. Express **23**(5), 6662–6672 (2015).
6. H. Gong, D. N. Wang, B. Xu, K. Ni, H. Liu, and C. L. Zhao, "Miniature and robust optical fiber in-line Mach–Zehnder interferometer based on a hollow ellipsoid," Opt. Lett. **40**(15), 3516–3519 (2015).
7. X. Hu, P. Mégret, and C. Caucheteur, "Surface plasmon excitation at near-infrated wavelengths in polymer optical fibers," Opt. Lett. **40**(17), 3998–4001 (2015).
8. X. Zhong, Y. Wang, C. Liao, S. Liu, J. Tang, and Q. Wang, "Temperature-insensitivity gas pressure sensor based on inflated long period fiber grating inscribed in photonic crystal fiber," Opt. Lett. **40**(8), 1791–1794 (2015).
9. Y. Liu, Y. Li, X. Yan, and W. Li, ""High refractive index liquid level measurement via coreless multimode fiber," IEEE Photonics Technol. Lett. **27**(20), 2111–2114 (2015).
10. X. Hu, D. Liang, J. Zeng, and G. Lu, "A long period grating for simultaneous measurement of temperature and strain based on support vector regression," J. Intell. Mater. Syst. Struct. **21**(10), 955–959 (2010).
11. C. Monteiro and S. Silva, "Hollow microsphere Fabry-Perot cavity for sensing applications," IEEE Photonics Technol. Lett. **10**(1109), 1–4 (2017).
12. H. Gao, H. Hu, Y. Zhao, J. Li, M. Lei, and Y. Zhang, "Highly-sensitive optical fiber temperature sensors based on POLYMER/silica hybrid fiber structures," Sens. Actuators, A **284**, 22–27 (2018).
13. R. Melamud, A. A. Davenport, G. C. Hill, I. H. Chan, F. Declercq, P. G. Hartwell, and B. L. P Ruitt, "Development of an SU-8 fabry-perot blood pressure sensor," *Proceedings of the IEEE International Conference on MEMS.*830 (2005).
14. C. Lee, L. Lee, H. Hwang, and J. Hsu, "Highly sensitive air-gap fiber Fabry–Pérot interferometers based on polymer-filled hollow core fibers," IEEE Photonics Technol. Lett. **24**(2), 149–151 (2012).
15. Y. Zhao, M. Chen, R. Lv, and F. Xia, "In-fiber rectangular air fabry-perot strain sensor based on high-precision fiber cutting platform," Opt. Commun. **384**, 107–110 (2017).
16. C. Luo and X. Liu, "An optimized POLYMER thin film immersed Fabry-Perot fiber optic pressure sensor for sensitivity enhancement," Coatings **290** (2019).
17. T. Liu, L. Hu, and M. Han, "Adaptive ultrasonic sensor using a fiber ring laser with tandem fiber bragg gratings," Opt. Lett. **39**(15), 4462–4465 (2014).
18. H. Bae, D. Yun, H. Liu, D. A. Olson, and M. Yu, "Hybrid miniature Fabry–Perot sensor with dual optical cavities for simultaneous pressure and temperature measurements," J. Lightwave Technol. **32**(8), 1585–1593 (2014).
19. S. Pevec and D. Donlagic, "Miniature all-fiber Fabry–Perot sensor for simultaneous measurement of pressure and temperature," Appl. Opt. **51**(19), 4536–4541 (2012).
20. K. Bremer and E. Lewis, "Conception and preliminary evaluation of an optical fibre sensor for simultaneous measurement of pressure and temperature," J. Phys. **178**, 346–350 (2009).
21. J. Ma, J. Ju, L. Jin, and W. Jin, "A Compact Fiber-Tip Micro-Cavity Sensor for High-Pressure Measurement," IEEE Photon. Technol. Lett. **23**(21), 1561–1563 (2011).
22. J. P. Dakin, W. Ecke, K. Schroeder, and M. Reuter, "Optical fiber sensors using hollow glass spheres and CCD spectrometer interrogator," Opt. Lasers Eng. **47**(10), 1034–1038 (2009).

Optics EXPRESS

23. Z. Ran and S. Liu, "Novel High-temperature Fiber-Optic Pressure Sensor Based on Etched PCF F-P Interferometer micromachined by a 157-nm Laser," IEEE Sens. J. **15**(7), 3955–3958 (2015).